Can we use topography to differentiate between area and discharge-driven incision rules, and if not how bad are our estimates of channel steepness?

Marina Ruiz Sánchez-Oro[1], Simon M. Mudd[1], and Boris Gailleton[2]

[1]School of GeoSciences, University of Edinburgh, Edinburgh, UK
[2]CNRS - Geosciences Rennes, Université de Rennes, France

Key Points:

- Discharge-driven incision can be identified *a posteriori* in simulated landscapes but not in natural topography.
- The choice of concavity index (θ) can distort the channel steepness index more than the choice of incision type.
- Topographic metrics should be accompanied by field explorations to fully describe the erosional history of a landscape.

Corresponding author: Marina Ruiz Sánchez-Oro, marina.ruiz.so@ed.ac.uk

Abstract

The rate of channel incision in bedrock rivers is often described using a power law relationship that scales erosion with drainage area. However, erosion in landscapes that experience strong rainfall gradients may be better described by discharge instead of drainage area. In this study we test if these two end member scenarios result in identifiable topographic signatures in both idealized numerical simulations and in natural landscapes. We find that in simulations using homogeneous lithology, we can differentiate *a posteriori* between drainage area and discharge-driven incision scenarios by quantifying the relative disorder of channel profiles, as measured by how well tributary profiles mimic both the main stem channel and each other. The more heterogeneous the landscape becomes, the harder it proves to identify the disorder signatures of the end member incision rules. We then apply these indicators to natural landscapes, and find, among 8 test areas, no clear topographic signal that allows us to conclude a discharge or area-driven incision rule is more appropriate. We then quantify the distortion in the channel steepness index induced by changing the incision rule. Distortion in the channel steepness index can also be driven by changes to the assumed reference concavity index, and we find that distortions in the normalized channel steepness index, frequently used as a proxy for erosion rates, is more sensitive to changes in the concavity index than to changes in the assumed incision rule. This makes it a priority to optimize the concavity index even under an unknown incision mechanism.

Plain Language Summary

Rivers erode into mountains as a result of both the sediment transported as the water flows downstream and the amount of water that the river transports. The amount of rainfall that each part of the river receives affects how much the channel cuts into the rock. In this study, we assess whether it is possible to differentiate between rivers where sediment is responsible for most of the erosion work and rivers where rainfall has a larger erosive power. Through computer simulations, we measure the river fingerprint in the landscape through calculations involving how tributary and main channel slopes compare, and how quickly a channel steepens as it travels away from the headwaters. We extract these fingerprints and search for them in the more complex natural landscapes, measuring how much they change under heavy rainfall. We find that these fingerprints are camouflaged by factors such as changes in rock types, making it a challenge to identify them without field observations.

1 Introduction

Physical intuition suggests that, if all other factors are equal, a steeper river will erode faster than a gentler one. This basic relationship has been proposed by geomorphologists for over a century (Gilbert, 1877). It is unusual, however, to find two channels identical in their properties with the exception of their gradient. Headwaters are, for example, frequently steeper than downstream rivers they feed. In the early 1960s geomophologists realized that gradient could be related to drainage area in a power law with a negative exponent (Hack, 1960; Morisawa, 1962). This basic relationship was formalized by Flint (1974):

$$S = k_s A^{-\theta} \tag{1}$$

where the concavity index, θ, describes how fast the gradient of the river changes downstream and the constant k_s, channel steepness index, describes the dependence of gradient normalized for drainage area. We can further fix the value of θ to a fixed reference value (θ_{ref}), after which we denote the channel steepness index with k_{sn}. This normal-

ization allows us to compare the relative steepness of rivers with different drainage areas (Flint, 1974).

Numerous studies have found that this relative steepness (k_{sn}) is positively correlated with measured erosion rates in upland landscapes (Wobus et al., 2006; DiBiase et al., 2010; Kirby & Whipple, 2012; Harel et al., 2016; Adams et al., 2020; Gailleton et al., 2021; Harries et al., 2021; Peifer et al., 2021). In regions without data on erosion rates we might therefore use k_{sn} as a proxy for erosion rate (Kirby & Whipple, 2012). This is not quite as straightforward as it sounds, however. If we return to physical intuition, consider two channels with all properties equal apart from the amount of water they convey (quantified as, e.g., their mean annual discharge or some other statistical representation of runoff). Many authors have proposed relationships between channel incision and the physical properties of bedrock rivers, and these proposals include the influence of sediment supply (dependent on A), sediment transport capacity (dependent on hydraulic conditions and gradient), shear stress (dependent on flow depth, and thus hydraulic conditions), stream power (again, hydraulic conditions), and thresholding behavior of all the above factors (Howard, 1987; Wobus et al., 2010; Finnegan et al., 2007; Johnson & Whipple, 2010; Baynes et al., 2020). This means that computation of k_{sn} based on drainage area rather than hydraulic conditions (e.g., discharge) may not represent the incision process.

One reason erosion rate proxies have tended towards using and area-based k_{sn} is because drainage area is trivial to extract form topographic data. Discharge (Q) records are not always easy to obtain, and gauging stations are at points rather than distributed throughout the landscape. However, various global datasets, for example TRMM (Kummerow et al., 2000) and GPM (Skofronick-Jackson et al., 2017) have made it relatively simple to estimate and aggregate precipitation over a basin, over a variety of timescales, which means it is now quite simple to obtain an estimate of discharge in a basin given a linear relationship between aggregate precipitation and discharge.

These precipitation datasets enable us to calculate the channel steepness index, k_{sn}, based on effective discharge rather than drainage area. And indeed, a number of recent authors have taken this approach (e.g., Babault et al., 2018; Adams et al., 2020; Leonard & Whipple, 2021; Harries et al., 2021; Leonard et al., 2023). If precipitation rates are uniform across a catchment, the drainage area-gradient relationship will have the same spatial pattern as the drainage area-discharge relationship. But rainfall can be influenced by mountains (Roe et al., 2002; Anders et al., 2006; Bookhagen & Burbank, 2006; Bookhagen & Strecker, 2008; Craddock et al., 2007; Gasparini & Whipple, 2014), meaning that the patterns of k_{sn} might be different if one uses A or a more direct estimate of Q that incorporates spatially varied precipitation.

One might assume that the latter is always "better" than the former. But there are some reasons why erosion rates, and gradients, might be more sensitive to drainage area than discharge. The main reason for this is that water does not erode the bed of rivers, sediment does. And the amount of sediment fluxing through any part of the channel in a steadily uplifting mountain range should depend on drainage area and not discharge. In addition, rivers transporting gravel will alter their geometry, for example their width (Dunne & Jerolmack, 2020; Phillips & Jerolmack, 2016; Pfeiffer et al., 2017), to accommodate sediment supply and this could cause a damping effect on the relationship between discharge and erosion rates. So although it intuitively might make sense to always use discharge-based calculations of k_{sn}, we are not, at present, certain if this is better than a calculation using A.

Any proposed erosion rule, be it area or discharge driven, can be transformed into a prediction of topography. For example, the most basic erosion law incorporating gradient and area of takes the form (Howard & Kerby, 1983):

$$E = KA^m S^n \tag{2}$$

where K is an erodibility and m and n are empirical coefficients. If one rearranges equation 2 to isolate S and compares the result with equation 1, one can see that, if equation 2 is correct, $k_{sn} = (E/K)^{1/n}$ and $\theta = m/n$. Thus equation 2 predicts a power law relationship between gradient and drainage area where erosion rates are invariant in time and space. It can also be shown that this power law relationship holds in segments of constant erosion that move upstream in transiently eroding landscapes (L. Royden & Perron, 2013). Various threshold models have been proposed as more complex versions of equation 2, but much of their relevant behavior can be captured by altering the n exponent (Gasparini & Brandon, 2011). While this approach is not without controversy (Lague, 2014), it is at least not clearly falsified by relationships between topographic data and measured erosion rates.

Such topographic predictions suggest a basic test: if there are strong gradients in precipitation, we expect the topographic outcomes of incision rules that are driven by either A or Q to differ. In this contribution we first explore the question: if we know erosion rates are driven by either A or Q, could we tell the difference just based on topography? We use numerical experiments to answer this question. We explore the extent to which heterogeneity in uplift rates and erodibilities can cloud this signal. Finally, we explore real landscapes to see if we can find locations, based on our proposed metrics, where it is clear that an area-based or discharge-based calculation of k_{sn} is more appropriate.

2 Methods

Our study includes three components. First, we perform a series of numerical experiments using a simple landscape evolution model with different imposed incision rules, and in addition alter other model parameters such as rainfall gradient. The aim of these simulations is to produce landscapes under idealized and controlled conditions against which metrics for determining the most likely incision rule may be tested. We then develop metrics that allow us to test if a particular incision rule better describes observed topography. Finally, we deploy these metrics on real landscapes.

2.1 Numerical simulations

We simulate landscapes where bedrock channels incise through an uplifting landscape. We thus must select an incision rule for our simulations. For the purposes of simplicity, we use the basic form of the stream power incision model (equation 2), which can emulate different incision mechanisms by altering the n exponent (Gasparini & Brandon, 2011).

Equation 2 is not influenced by discharge. For discharge-based incision, we follow other authors (e.g. Adams et al., 2020) and replace drainage area with a proxy for discharge, which we compute with the substitution $Q = A \times Rainfall$ where the rainfall is converted into runoff and accumulated downstream, yielding:

$$E = K_{lp} Q^m S^n. \tag{3}$$

In reality, the discharge will be modulated by other features such as evapotranspiration and infiltration rates, but these factors are subsumed into the parameter K_{lp}.

The model then simulates topographic evolution with a simple mass balance:

$$\frac{\partial z}{\partial t} = U - E \tag{4}$$

where U is the uplift rate and the erosion rate, E, is solved by either equation 2 or 3. Simulations are performed using the Fastscape framework (Bovy & Lange, 2023). Fastscape uses the methods developed by Braun and Willett (2013) that takes advantage of graph theory to efficiently solve equations 2 (or 3) with an implicit finite different scheme.

In order to implement equation 3, we must assign a precipitation pattern. In our experiments, we explore different precipitation gradients. Models do exist where precipitation depends on elevation and prevailing wind direction, for example the model of Smith and Barstad (2004) which was used by Han et al. (2015). Such models involve multiple parameters, and to obtain the desired precipitation gradient one must engage in fine tuning each of these parameters. For consistency across experiments, we decided instead to increase precipitation linearly as a function of distance from the mountain front, with precipitation gradients comparable to real orographic rainfall gradients. Leonard and Whipple (2021) found that a linear rainfall gradient can be a good approximation to studying orographic precipitation patterns in natural landscapes.

We impose rainfall gradients that will mimic natural orographic patterns found in natural landscapes. In the driest scenario, we impose a rainfall gradient across the simulated mountain range of 1 m/yr (that is, the precipitation is 1 m/yr greater at the peak rainfall location than at the minimum rainfall location). In our wettest scenario, the increase in rainfall reaches 10 m/yr across the simulation domain, corresponding to the highest rainfall achieved in the Bhutan Himalayas (Grujic et al., 2018; Anders et al., 2006).

2.1.1 Homogeneous Lithologies

We run experiments on a regular grid ($\Delta x = 30m$) grid over a mountain range that is 15 km by 30 km (see Table 1 in S1 for full parameter details). This size was selected as a compromise between the number of basins that could be formed during a simulation and computational expense. We begin each landscape with a random surface generated using the diamond square algorithm (Fournier et al., 1982; Perron & Royden, 2013) with noise ranging from 0 to 1 m. We choose this initial condition as it produces a greater variety of channel network structures than the more widely used white noise. Each simulation is run to steady state, where the change in erosion is balanced by uplift.

For a given uplift and precipitation gradient, we calculate the landscape resulting from each of the two incision laws as described by equations 2 and 3. Initial experiments use uniform erodibility to simulate homogeneous lithology. The boundary conditions include a fixed elevation on the east and west edges (which allow flux to exit the model) and periodic boundaries at the north and south of the model domain. The resulting mountain range emerges in the North-South direction.

Within the discharge-driven model, we set up one simulation for each rainfall scenario, starting from a gradient of 0 m/yr to to 10 m/yr (increasing from East to West in the simulation domain), for a total of 11 simulations. The precipitation runs explore how different rainfall amounts affect river incision mechanisms and whether larger gradients generate a stronger signal in the landscape.

Both the erodibility coefficient and the uplift rate are kept constant across all simulations at 3×10^{-8} and uplift rate is 1×10^{-5} respectively, yielding landscape reliefs within the ranges of those found on Earth. Similarly, n is chosen as 1 and m as 0.45 to keep the m/n ratio equal to 0.45, which is the central tendency of the concavity index across a large number of global landscapes (Kirby & Whipple, 2012; Gailleton et al., 2021; Tucker & Whipple, 2002). Although n is thought to take values other than unity in most landscapes (Lague, 2014; Harel et al., 2016), the value of this parameter is only man-

ifested in topographic outcomes during landscape transience (Whipple & Tucker, 1999; L. Royden & Perron, 2013) and does not affect our simulations since the landscapes are brought to steady state. When studying the channel steepness index across multiple basins, we set a reference value, θ_{ref}, (Gailleton et al., 2021) of 0.45 to establish a comparison between basins.

2.1.2 Heterogeneous Lithologies

To study the role of lithology in the prevalence of rainfall patterns we run a set of simulations with spatially varying values of erodibity, K. These simulations are designed to be closer to natural landscapes where the lithological landscape is more complex.

Within this study, we choose two lithological units reflecting the properties of a harder and a softer rock, with erodibility values ranging between $1e{-}7 < K < 5e{-}8$. This is in line with (Forte et al., 2016; Bernard et al., 2021; Peifer et al., 2021). Peifer et al. (2021), which determined that hard rocks can be related by a factor from 2-10 in erodibility to softer rocks (Forte et al., 2016; Bernard et al., 2021).

We simulate three heterogeneous lithologies scenarios: striped (a), sparse blob (b) and dense blob (c) lithologies (see SI, Figure S1).

1. **Striped lithology:** band of hard rock ($K = 5e - 8$) in the center of our simulated mountain range, surrounded by soft rock ($K = 1e - 7$) to emulate cases like the Pyrénées.
2. **Sparse blob lithology:** 4 large hard rock ($K = 5e{-}8$) blobs evenly distributed on the landscape domain.
3. **Dense blob lithology:** many small hard rock blobs ($K = 5e{-}8$) of a few square meters in diameter, generated using Perlin noise (Perlin, 1985).

2.1.3 Natural Landscapes

We have chosen natural landscapes for this analysis on the basis of precipitation gradients and lithological structure, avoiding areas that have complex layers of soft rocks (Table 1). We analyze basins with a minimum drainage area of $1e7m^2$. We incorporate all channel pixels within tributaries that have a source area greater than $1.35km^2$ (which corresponds to 1500 pixels in topographic data with 30 m grid spacing).

Table 1. Geographical areas chosen along with the number of selected basins in each regions, area and rainfall range across the basin, from the outlet to the headwaters of the catchment. We choose a varied range of area sizes and precipitation gradients with to study prevalent trends across regions. Data extracted from the 30m Copernicus DEM and NASA's Global Precipitation Measurement Mission (GPM) (Skofronick-Jackson et al., 2017).

Location	N basins	Area (km^2)	Precipitation Range (m/yr)
Andes, Southern Perú	5	29979	0.687-3.983
Andes, Northern Argentina	7	5932	0.045-0.010
North Qinling Mts, China	14	30832	0.734-0.938
Kaçkar Mts, Turkey	8	4279	0.784-1.673
Colorado Front Range, USA	7	9282	3.726-4.220
Alburz Mts, Iran	7	8167	0.357-0.849
Massif Central, France	5	1945	0.977-1.092
Pyréneées, Spain-France	5	6632	0.097-0.117

2.1.4 Varying the simulation concavity index, θ (i.e. m/n ratio)

We assess the impact of running the homogeneous lithology simulation with a further two choices of m/n: 0.35 and 0.55. The rationale for these experiments is to determine if changes to the imposed m/n ratio causes distortions to k_{sn} of the same magnitude as those induced by changing the incision rule. The broad effect on the landscapes with different values of m/n compared to the base case of $m/n = 0.45$ is that at 0.35 the landscape is smoother with lower relief and higher drainage density with sinuous tributaries, whereas at $m/n = 0.55$ the landscape has sharper features, with higher relief and lower drainage density, forming straighter tributaries. For detailed results of these simulations, see SI (Text S6, Figures S16-S19, Tables S8-9.

2.2 Metrics to quantify topographic outcomes

Our models simulate river incision, and so we use river profiles to explore topographic outcomes of simulations. Because gradients should scale by either A or Q (depending on the incision rule) we use a coordinate transformation, first proposed by (L. H. Royden et al., 2000), that integrates either A or Q along the river profile:

$$\chi_A = \int_{x_0}^{x} \left(\frac{A_0}{A(x)} \right)^{\theta} dx \tag{5}$$

$$\chi_Q = \int_{x_0}^{x} \left(\frac{Q_0}{Q(x)} \right)^{\theta} dx \tag{6}$$

This transformation has various useful features. The gradient in χ_A–elevation space is equivalent to k_s if $A_0 = 1$ m^2 (e.g., Perron & Royden, 2013; L. Royden & Perron, 2013; Mudd et al., 2014), and the gradient in χ_Q–elevation space is equivalent a metric k_{s-q} where gradient is scaled by Q instead of A in the form:

$$S = k_{s-q} Q^{-\theta} \tag{7}$$

when Q_0 = unity in the units of Q used to calculate both χ_q and k_{s-q} (e.g., Adams et al., 2020; Leonard et al., 2023; Leonard & Whipple, 2021; D'Arcy & Whittaker, 2014; Harries et al., 2021). These steepness metrics can be used both in steady state and transient landscapes (L. Royden & Perron, 2013). Another advantage of using the χ transformation is that tributaries to the main channel at the same elevation yield the same χ value, regardless of their drainage area. Given a landscape in steady state, the main channel and its tributaries should follow the same linear relationship on a χ–z plot, assuming the same erosion and uplift rates (Perron & Royden, 2013) and the optimal concavity index value.

We exploit this latter feature in our efforts to discriminate, topographically, between incision rules. Regardless of the incision rule, selection of the incorrect value of θ will result in tributaries that are not collinear, introducing distortions in channel steepness index (Perron & Royden, 2013; Mudd et al., 2018; Hergarten & Robl, 2022; Gailleton et al., 2021; Goren et al., 2014; Harries et al., 2021). Computing χ_A or χ_Q also affects the channel steepness index values and the spread of the data, which can lead to different patterns of the channel steepness index and spreading the data in χ space (Figure 1). Because k_{sn} values are used to infer relative erosion rates across tectonically active regions, distortions to the spatial patterns of the channel steepness index can cloud interpretations of topographic pattern (e.g., Gailleton et al., 2021).

We quantify the spread of the χ–z profiles using a disorder metric, first proposed by Goren et al. (2014) and further developed by Hergarten et al. (2016) and Mudd et

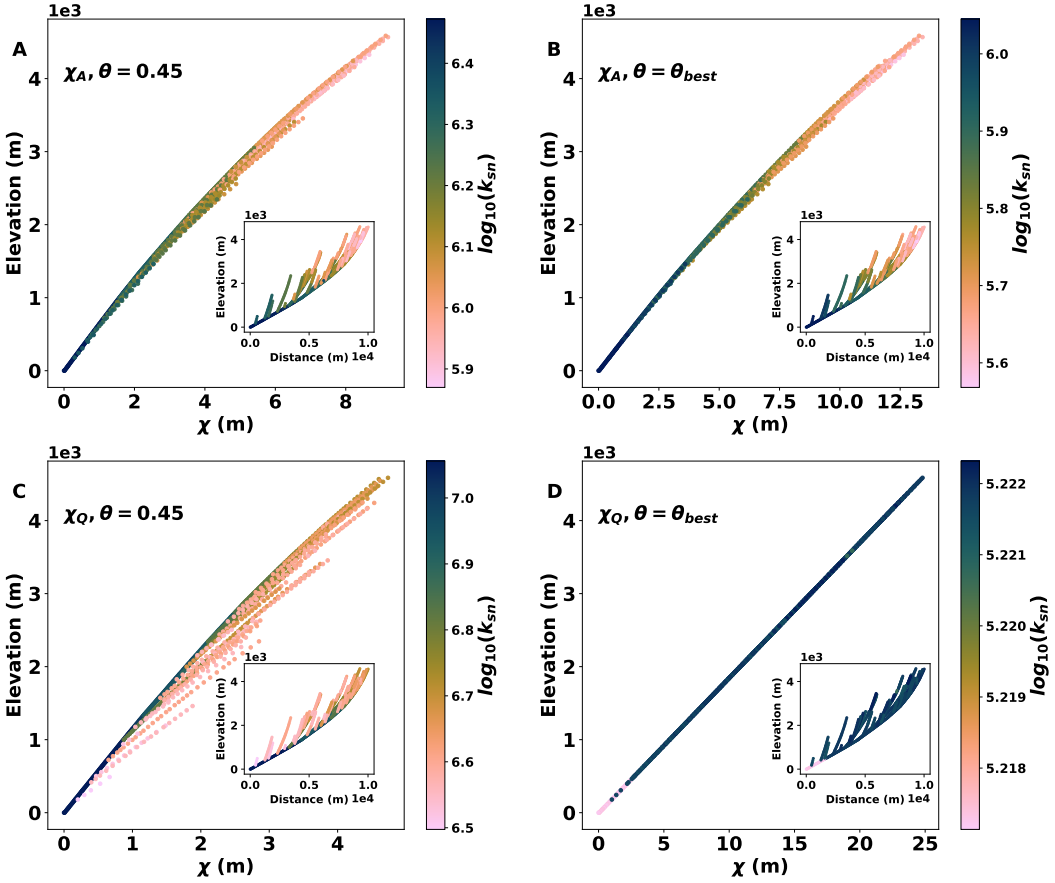

Figure 1. Illustration of how χ profiles and k_{sn} change based on the choice of incision scenario and concavity index values. The χ profiles result from simulations with a range of precipitation of 10m/yr (increasing west to east) under initial m/n=0.35. The basin shown is located on the wetter side of the domain, draining to the east. (D) shows perfect collinearity under χ_q and θ_{best}, which match the simulation parameters. (A) shows distortions using both the incorrect incision rule and the wrong θ, (B) shows a slightly more collinear profile, in this case only having the incorrect incision. (C) captures the correct incision (discharge) but uses θ=0.45, where we see the largest increase in disorder and changes in k_{sn}.

al. (2018). One begins by ranking every point in the channel network by increasing elevation, and then checks to see if the associated χ coordinates are similarly ranked (or not):

$$R = \sum_{i=1}^{N} \left| \chi_{s,i+1} - \chi_{s,i} \right|, \tag{8}$$

where the the subscript s, i represents the i^{th} χ coordinate that has been sorted by its elevation ($\chi_{s,i}$). This sum, R, is minimal if elevation and χ are related monotonically. However it scales with the absolute values of χ, which are sensitive to the concavity index (see equations 5 and 6), so following Hergarten et al. (2016) we scale the disorder metric, D, by the maximum value of χ in the tributary network (χ_{max}):

$$D(\theta) = \frac{1}{\chi_{max}(\theta)} \left(\sum_{i=1}^{N} \left| \chi_{s,i+1}(\theta) - \chi_{s,i}(\theta) \right| - \chi_{max}(\theta) \right). \tag{9}$$

We use the method of Mudd et al. (2018) to constrain uncertainty of this metric by creating subset networks formed from the trunk stream and every possible combination of three tributaries in a particular basin. This creates a population of D values for a given basin from which a median and interquartile range may be reported.

We normalize the disorder values across all tributary combinations, obtaining:

$$D^*(\theta) = \frac{D(\theta)}{D_{max}(\theta)} \tag{10}$$

where D_θ is the disorder for each tributary combination and $D_{max}(\theta)$ is the maximum disorder over all combinations.

In our analysis we aim to decipher whether we can identify the signal from a landscape shaped by rainfall *a posteriori*. To quantify this, we focus on the effect of rainfall in the $\chi - z$ profiles and in the disorder metrics. To emulate what the analysis would look like if we did not know the incision rule, we calculate the χ profiles in two ways for each simulation scenario - regardless of what the actual imposed incision rule is for a given numerical experiment. We calculate these metrics for each basin in the simulation draining to the edge and reaching the main drainage divide (Figure 2). For each of the basins simulated in each model scenario, we calculate the following:

1. χ_A: assumes a drainage area-driven incision (equation 5).
2. χ_Q: assumes a discharge-driven incision (equation 6).

For each of the χ cases, we calculate the disorder metric (equation 9). The disorder constrains the value for the optimal concavity index, θ_{best}, that will lead to the most collinear river profile configuration (Mudd et al., 2018; Gailleton et al., 2021).

2.3 Statistical Analysis

For each incision scenario, we calculate minimum normalized disorder values ($D^*(\theta)$) corresponding to each of the basins under each of the incision and χ scenarios. To measure if $D^*(\theta)$ for the basins in the simulations where incision is purely a function of A is statistically distinguishable from the basins where incision is driven by Q, we extract the value for $D^*(\theta)$ for each basin and χ case. We then calculate the absolute error between $D^*(\theta)$ in the two χ cases. The true value corresponds to calculating $D^*(\theta)$ with the χ of the matching incision scenario. The distribution of error values (ΔD^*) for all basins for each incision case can then be expressed as:

$$\Delta D^* = D^*_{rain} - D^*_{norain} \tag{11}$$

Since we are dealing with non-parametric distributions, we take the median of ΔD^* to quantify whether the A-based incision models may be distinguished from the Q-based incision models. We represent the distributions with kernel density estimates (KDE) (Cox, 2007; Silverman, 1998). If a percentage smaller than 5% is shared between the two distributions we consider them to be distinguishable from each other with 95% confidence.

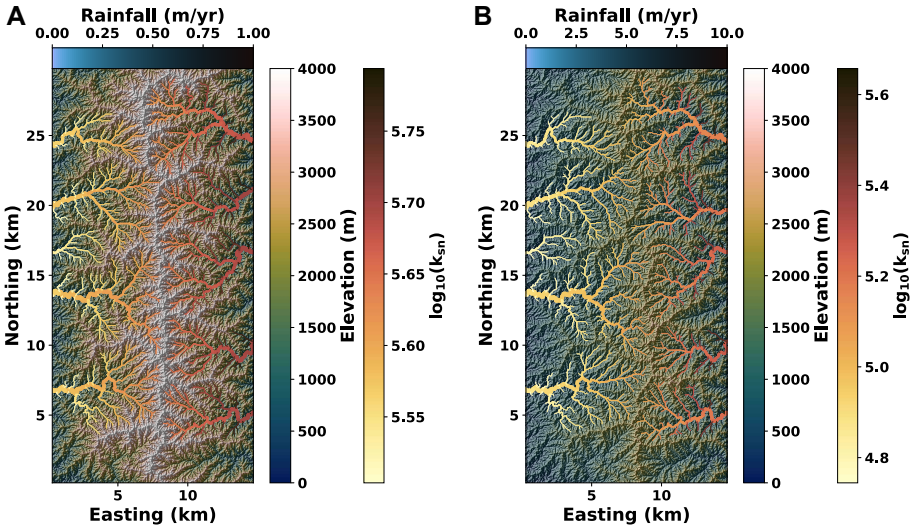

Figure 2. River networks generated with the numerical model under two discharge-driven incision scenarios, with rainfall ranges between (A) 0-1m/yr and (B) 0-10m/yr in the East-West direction. The smaller rainfall ranges in (A) lead to higher relief, steeper channels and a symmetric drainage divide. The higher rainfall in (B) leads to lower relief and a more sinuous and asymmetric drainage divide.

2.4 Measuring the effects of rainfall and θ on k_{sn}

In our numerical landscapes, we impose an erosion rule and then quantify the extent to which profiles are disordered when applying the appropriate or incorrect χ transformation (that is, using either A or Q). In real landscapes, however, we can only infer which of the two χ transformations is correct based upon relative disorder, and indeed neither may be correct. We resort to distortion in the χ–elevation profiles to quantify the impact of the choice of A or Q to scale χ when the correct choice is unclear. Specifically the distortion metrics quantify the degree to which k_{sn} changes if different choices in calculating χ are made. Determining the distortion of k_{sn} due to the choice of A or Q in calculating k_{sn} is important because it can affect the interpretations of the tectonic and erosional history of a landscape (Kirby & Whipple, 2012).

We quantify distortion by calculating the ratio between median upstream and downstream k_{sn} values and then investigating how this ratio varies depending on concavity index (Case *i*), incision scenario (Case *ii*) or both (Case *iii*), following the methods in (Gailleton et al., 2021). A full derivation of equations used to calculate the distortion is included in the SI, Text S1.

3 Results

In this section we present the numerical experiments and explore the effects of rainfall gradient on channel steepness and concavity index. We cover both homogeneous and heterogeneous lithologies.

3.1 Homogeneous lithology

3.1.1 Drainage area or discharge-driven incision?

Figure 3 shows the distributions of ΔD^* in each experiment using KDE fitting for Q-driven incision rule (equation 3) and A-driven incision rule (equation 2). Each kernel estimate is obtained for the collection of basins in the simulated domain. We obtain the median (solid line), 95th and 5th (dashed lines) percentiles for each kernel, repeating this procedure for each of the rainfall gradients. We consider $\Delta D^* = 0$ as the point where calculating χ_Q or χ_A would have no effect on the minimum disorder.

Figure 3 shows the distribution of ΔD^* values. Basins where the χ and the incision scenario match have lower D^* values. This is represented by the A-driven distributions lying on the negative side of the x-axis, meaning that the disorder value calculated using χ_A is lower than the disorder calculated using χ_Q. That is, unsurprisingly, using the version of χ that corresponds with the imposed incision rule results in less disordered channel profiles. The opposite is true of the Q-driven basins, which lie on the positive x-axis range, where the disorder is lower when calculating χ_Q than χ_A. This is true of all three indicated metrics: median, 95th and 5th percentiles. None of the distribution tails overlap inside of the 5-95th percentile ranges. For every rainfall distribution illustrated, the drainage area and the discharge driven incision are statistically far enough apart to be considered distinct distributions.

As rainfall gradients increase, the medians of the distributions diverge. For smaller rainfall gradients, the distribution medians appear closer together but still outside the 95% of each other that we consider an indication they are statistically distinct. The most significant differences arise from the discharge-driven scenarios, with the changes in the drainage area ΔD^* evolving slower with increased rainfall.

For every rainfall distribution illustrated under homogeneous lithology, calculating χ_Q or χ_A leads to statistically distinct ΔD^* distributions for the A and the Q-driven scenarios. Disorder can thus be used as a tool to recognize the dominating incision rule in numerical simulations: when $\Delta D^* < 0$, the incision is drainage area-driven, whereas $\Delta D^* > 0$ implies that discharge is the main incision mechanism.

3.1.2 k_{sn} distortion

We quantify k_{sn} distortion based on the cases outlined in section 2.4. We remind the reader of the three distortion cases we consider in this study *i*) change in θ, *ii*) change in incision rule, and *iii*) change in both. Similar patterns in changes in k_{sn} can arise from either of the three cases.

Figure 4 illustrates each of the distortion cases along a series of rainfall gradients for the discharge simulations. Panels A and B correspond to changes in θ (Case i). Panel C represents a change in incision rule (Case ii) and Panel D reflects a combined change in incision rule and θ values (Case iii). In all plots we indicate the no-distortion scenario at $y = 0$ with a solid black line.

Figure 4A reflects data from k_{sn-q} calculations, which capture the rainfall range used for the discharge-driven simulations. The associated distortion remains close to 1, indicating that using $\theta = 0.45$ as opposed to θ_{best} has minimal effects in the basin-averaged k_{sn} values. This can be explained by referring to the model set up. In the discharge-driven model with $m/n = 0.45$, with no other external factors to disturb equilibrium, we obtain steady state channel profiles with $\theta_{best} = 0.45$. This value is obtained from disorder minimization including rainfall in the calculations. Figure 4B reflects the results of not including a rainfall range in the disorder minimization procedure when calculating θ_{best}. Starting with a null distortion for the 0 m/yr rainfall range, distortion gradually increases with rainfall ranges. The distortion values reach 23% where $\theta_{best} > 0.45$

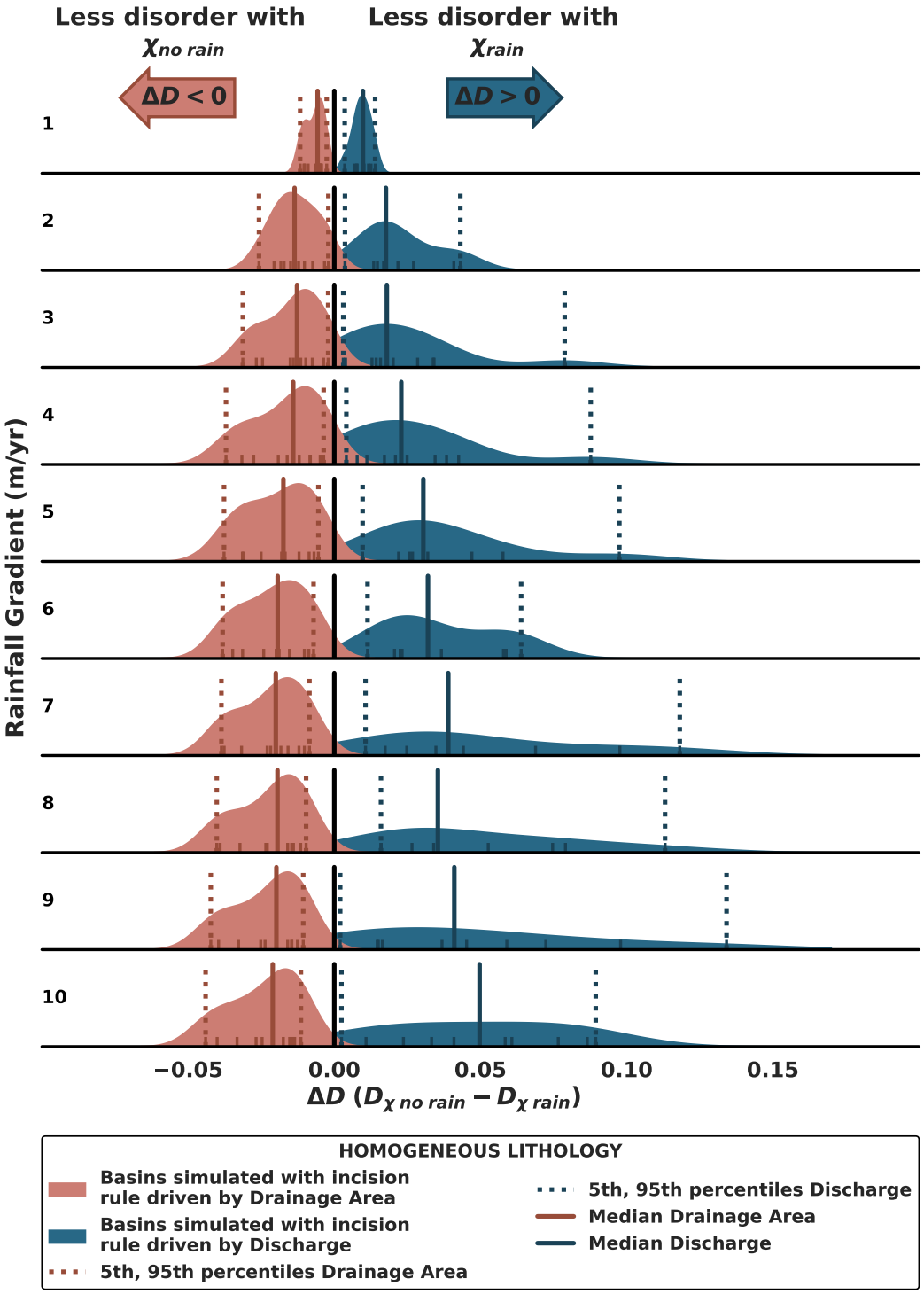

Figure 3. Comparison of the median values for ΔD^* for each of the rainfall gradients for A and Q-driven incision under homogeneous lithology for an initial m/n=0.45. The two models are always distinguishable: each of the distributions is on either side of the 0 line, with 95% confidence. The larger the rainfall gradient, the more separated the distribution medians become.

(above 1) and 15% when $\theta_{best} < 0.45$ (below 1). As the rainfall range increases, θ_{best} values diverge from 0.45. Figure 4C shows the distortion in case ii, which results from a difference in the assumed incision rule at a fixed concavity index ($\theta = 0.45$). The distortion pattern follows a similar path to Figure 4B: as rainfall ranges increase, so does the k_{sn} distortion. In this case, the values > 1 correspond to the windward (wetter) basins, where rainfall decreases as we move towards the mountain range. Distortion < 1 corresponds to leeward (drier) basins where rainfall decreases as we move away from the mountain range. In both cases, distortion reaches 11%, with differences originating from the magnitude and the direction of the rainfall gradient. Figure 4D depicts distortion case iii: the effects of both a change in θ and a change in the incision rule. The percentage of k_{sn} distortion is larger than in the other three scenarios: a 34% increase at the highest point against 23% and 11% in Figure 4B and C respectively. This arises from the basins having different θ_{best} depending on the incision rule used to calculate the k_{sn} distortion. The effect in the distortion is additive, meaning that compared to the correct case for both incision and θ ($k_{sn-q}(\theta = \theta_{best})$), optimizing θ for the wrong incision case would lead to the greatest distortion out of the three cases considered.

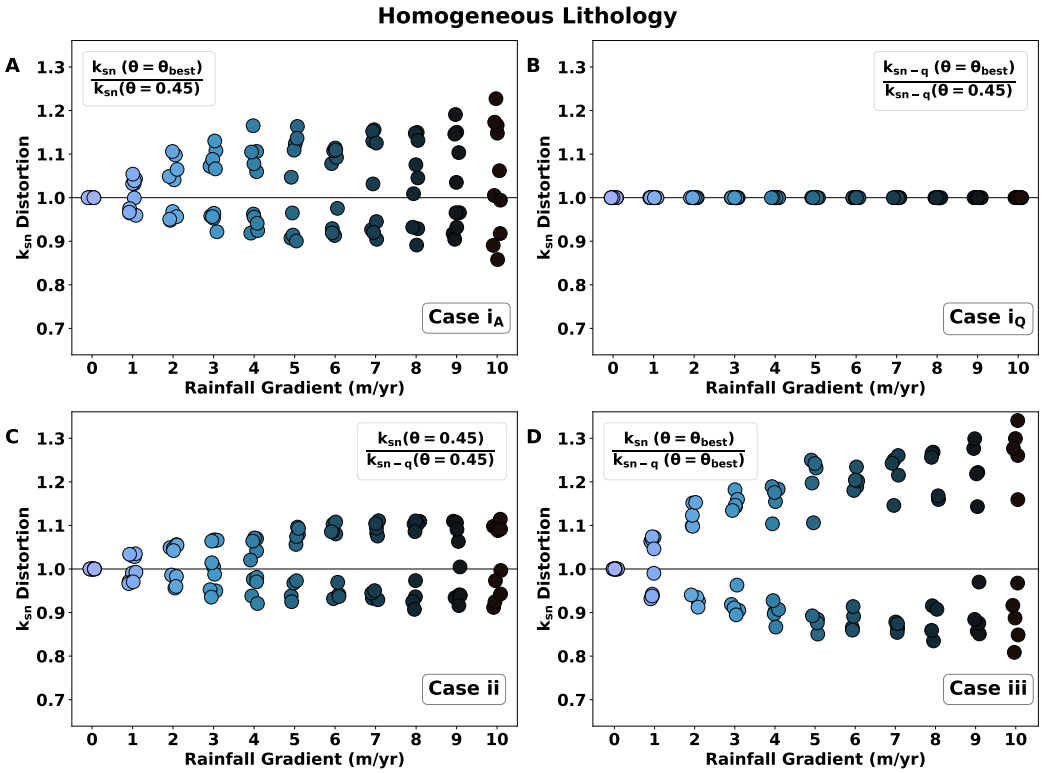

Figure 4. Distortion in k_{sn} for the Q-driven incision case under homogeneous lithology and initial m/n=0.45. A distortion of 1 (solid black line) keeps the value of k_{sn} unchanged. (B, Case i_Q) indicates that no k_{sn} distortion occurs when the concavity index and the incision case match the model scenario. (A), (C) and (D) show the possible distortion scenarios that one might encounter under different assumptions. (A) highlights the effects of optimizing concavity index under an incorrect incision scenario, (C) assumes concavity index is kept at 0.45 but the incision scenario changes and (D) comprises the effects of θ optimization under different assumptions of incision scenarios, where we see the largest k_{sn} distortions of up to 34%.

Distortion in the channel steepness index can be caused both by incorrectly assuming concavity indices and incorrectly assuming incision rules. That is, to calculate k_{sn} one must set a value of θ, and one must choose whether or not to incorporate a proxy for discharge, and either of these assumptions may not be the best reflection of reality in any given landscape. optimizing θ will decrease the distortion in k_{sn} values, for cases when the incision mechanism is unknown. If we identify an incision mechanism, then distortion can also be decreased by using either k_{sn} or k_{sn-q}, depending on the case. However, we find that optimizing θ for an incorrect incision case leads to the highest distortion values.

3.2 Heterogeneous lithology

We have shown that it is possible to differentiate a signal from an A-driven incision scenario from a Q-driven scenario, under homogeneous lithology. However, many natural landscapes contain a range of lithologies with different erodibilities. We complement our analysis with data from simulations with heterogeneous lithologies, as described in Section 2.1.2. We illustrate the behavior from results from the most densely varying lithology (dense blob), with two extra cases (blob and striped lithology) included in the Supplementary Information.

In Figure 5 we see that in contrast with the homogeneous lithology case, we see that the disorder metrics derived from the A-driven and Q-driven basins are not statistically distinct. Both distribution medians are similar regardless of the rainfall range and they fall within each other's 95% percentile of the population. The more heterogeneous the erodibility, the harder it becomes to distinguish between the original incision rules. The dense blob lithology simulations feature channel metrics where it is most difficult to differentiate A-driven from Q-driven incision rules using, with other lithologic types having larger differences in median disorder (see Supplementary Information).

We also quantify how heterogeneous lithologies impact the distortion of k_{sn} values. We start by looking at the result of adding lithology to the discharge-driven model scenario and compare the results to Figure 4. We highlight that in the heterogeneous lithology cases, we do not expect θ to be 0.45 at a rainfall range of 0m/yr. We have introduced a perturbation, leading the system to diverge from $\theta = 0.45$ that we obtained in an unperturbed, steady state scenario. This is reflected in a distortion between 10% - 20% at rainfall ranges of 0 m/yr in all distortion cases. Irrespective of the range in rainfall, this distortion remains within the same bounds. We see consistently higher distortion values for all rainfall ranges in 6B, as a result of using the incorrect incision scenario when optimizing θ. In Figure 6C we see the distortion associated with Case ii (caused by changes in incision rule), when keeping $\theta = 0.45$. As the rainfall range increases, the distortion shifts towards being larger, up to 44% in leeward basins. When we optimize θ and compare between the two incision scenarios 6D, the distortion in both the windward and the leeward side is increasing at a similar rate with increasing rainfall ranges. This is the only distortion case where we see a systematic increase in distortion with rainfall ranges.

Heterogeneities in lithology add to the distortions in channel steepness index caused by rainfall ranges. The signal from the rainfall is reflected as a systematic increase in distortion in A-driven cases. In Q-driven scenarios the systematic increase of distortion with rainfall range is masked by the lithological heterogeneities when comparing between θ values. optimizing θ will remove the distortion that we incorporate by using $\theta = 0.45$, which is more prominent in heterogeneous than homogeneous lithologies. Making a decision on the type of incision, will also reduce the distortion. However, this can end up with an increased distortion if the incision type assumed for calculating χ is incorrect and θ is subsequently optimized using channel information obtained from that incorrect incision type.

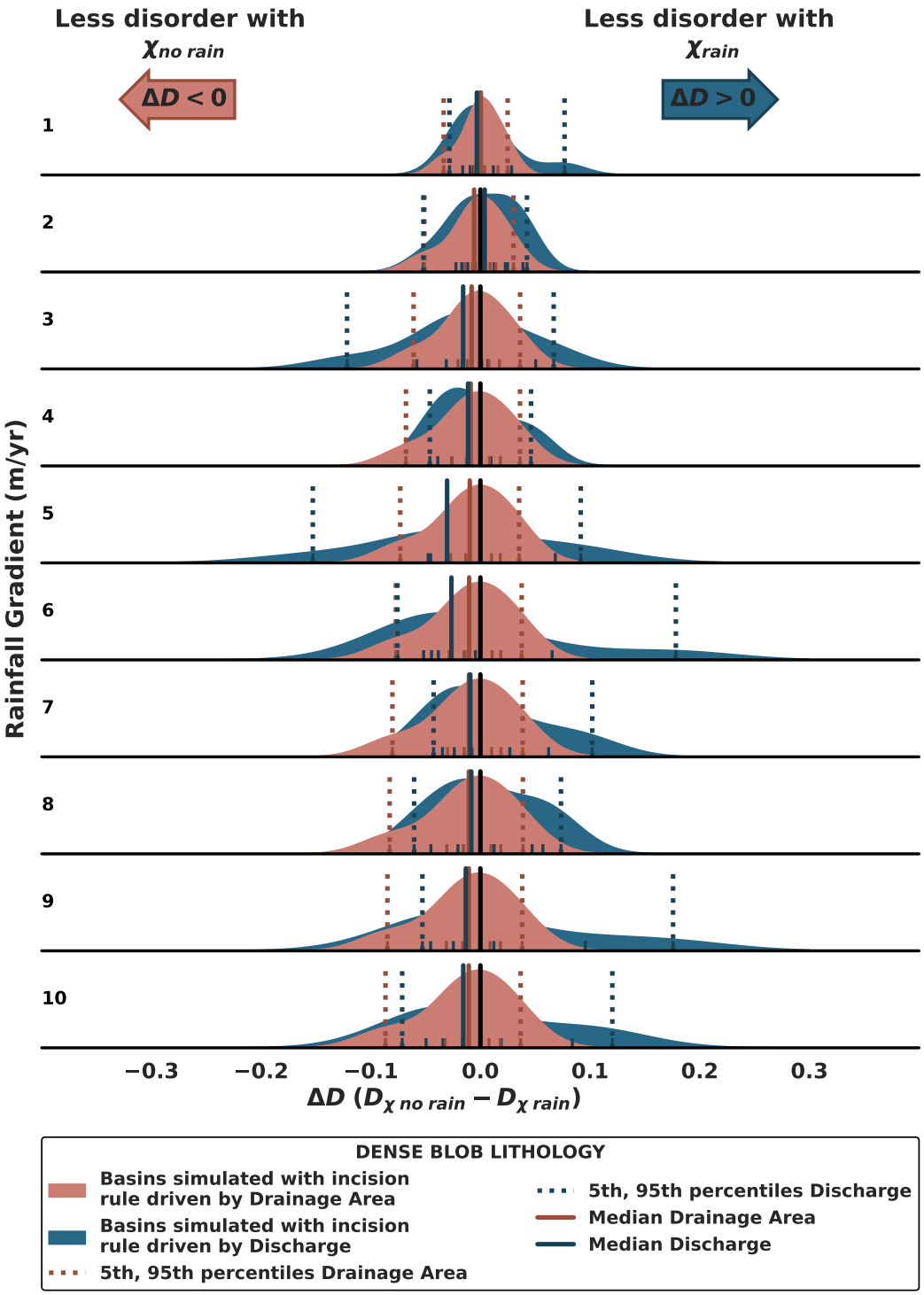

Figure 5. Comparison of the median values for ΔD^* for each of the rainfall ranges for A and Q-driven incision under dense blob lithology for an initial m/n=0.45. The distribution medians and percentiles largely overlap, meaning that the models are not distinguishable, regardless of the rainfall gradient.

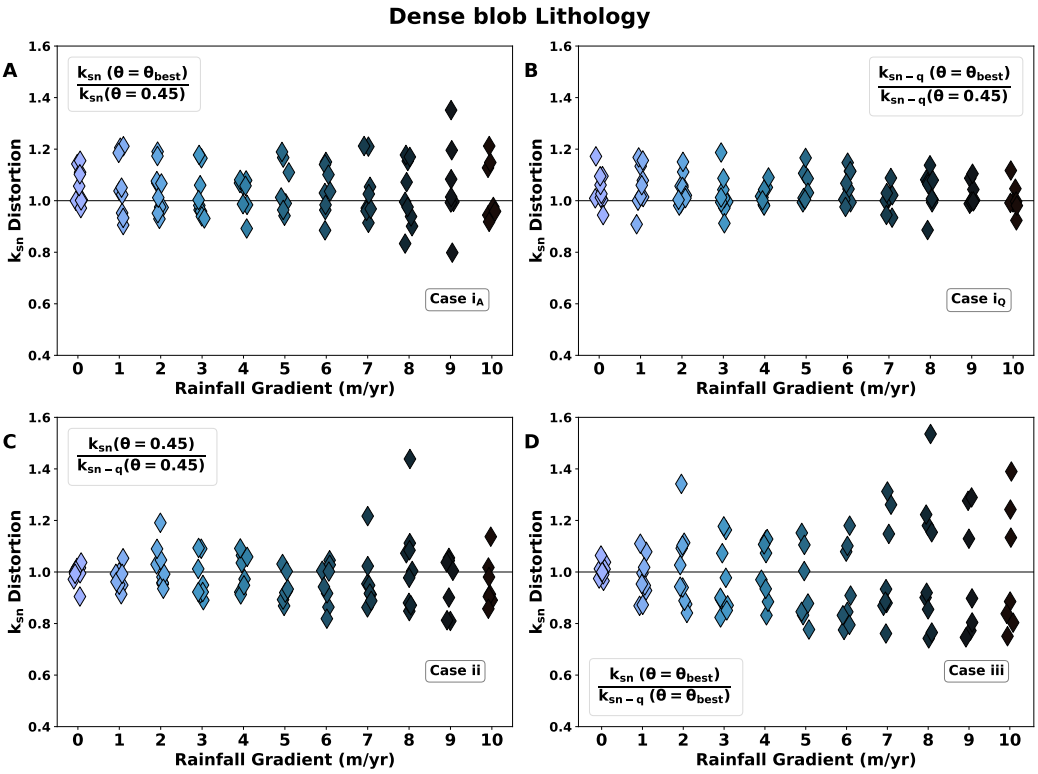

Figure 6. Distortion in k_{sn} for the Q-driven incision case under heterogeneous lithology and initial m/n=0.45. A distortion of 1 (solid black line) keeps the value of k_{sn} unchanged. We show the possible distortion scenarios that one might encounter under different assumptions of concavity index and incision. (A) highlights the effects of optimizing concavity under the incorrect incision scenario (drainage area), whereas (B) shows the distortion incurred by not optimizing θ under Q-driven incision. (C) keeps concavity index at 0.45 but compares incision scenario and (D) comprises the effects of θ optimization under different assumptions of incision scenarios, where we see the largest k_{sn} distortions of up to 54%.

3.3 Natural Landscape Study Cases

We have quantified how a changing range of rainfall can lead to differences in k_{sn} and θ_{best} under various incision scenarios in simulated landscapes. Our numerical experiments suggest that it is possible to statistically distinguish A-driven and Q-driven incision landscapes in a lithologically homogeneous model using disorder metrics. Heterogeneous lithologies capture how the rainfall signal is obscured by additional forcings, namely spatial variation in erodibility, a common feature in natural landscapes. Having isolated these signals in experiments, we now apply this knowledge to real landscapes, where we only have *a posteriori* topographic states from which to infer the landscape incision rule. We remind readers, when interpreting our results, that $D^*(\theta_{best,Q}) < D^*(\theta_{best,A})$ suggests that the basin has been shaped by rainfall as a main incision mechanism. On the other hand, $D^*(\theta_{best,Q}) > D^*(\theta_{best,A})$ suggests that basin incision is driven by drainage area. Our numerical experiments suggest that $\Delta D^* < 0$ in landscapes with A-driven incision. In Q-driven, $\Delta D^* > 0$. We calculate ΔD^* for natural landscapes in the same fashion.

For each basin, we repeat the calculations outlined in section 2.2, and plot the median values of normalized distortion (ΔD^*) and their distributions in Figure 7. As a reminder, this metric quantifies which of the two assumed incision scenarios results in lower distortion of the channel network. If all basins are positive, or all are negative, we view this as an indication that one of the two assumed incision signals better describes the observed topographic data. We see in Figure 7, most natural landscapes have basins that straddle $\Delta D^* = 0$, meaning that we cannot determine the most likely incision scenario with any confidence. Only in the cases of the Colorado Front Range and the Massif Central do we see a statistically significant imprint on ΔD^*. Those basins lie on the positive side of the x-axis, favoring discharge as the predominant incision mechanism. The other sites show smaller confidence intervals in ΔD^* values, and their basins only a slight trend towards an incision scenario (drainage area -Pyrénées, Alburz, Qinling- and discharge -Perú, Argentina, Kaçkar-). The distributions center largely around the $\Delta D^* = 0$ with spreads at either side of the incision case division.

If we are not able to distinguish the correct incision scenario using the disorder metrics, how uncertain will our interpretations of channel steepness become? In Figure 8 we investigate distortions in the channel steepness index. We highlight the difference in scale of the results shown here. In the modeling experiments, some scenarios show a distortion of no more than 10% under low rainfall (eg. Figures 4A, S12B, S3 (A-C)). In real landscapes, we observe larger distortion values for all cases, in some instances reaching 36% in 8D, 50% in 8B and above 75% distortion in 8A and C. In natural basins, using $\theta = 0.45$ becomes a large source of distortion to the channel steepness index, regardless of the assumed incision scenario. This is a consequence of the θ_{best} values diverging from 0.45, which corresponds to the m/n value of the models. Compared to these large distortion values incurred by using $\theta = 0.45$, the distortion values arising from choosing A-driven or Q-driven incision scenarios fall considerably. We see most distortion falls within the 25% bounds, regardless of the mountain range, although with different amounts of spread around the null distortion line at $y = 1$. This shows that in natural landscapes, optimizing the concavity index is more important than choosing the correct incision scenario. As opposed to the model, in natural topography we do not see an increase in the distortion originated from case *iii* compared to the other two cases.

We plot the distributions of k_{sn} and k_{sn-q} for θ_{best} and $\theta = 0.45$. Under $\theta = 0.45$ (9B), the differences in channel steepness index are larger, for instance in Argentina or Colorado, were the peak of the distribution is shifted and the distributions changing shape. However, cases such as the Pyrénées or the Massif Central show little differences in the distributions. 9A shows the channel steepness index distributions for θ_{best}. We see that the shape of the curves is better preserved, with less variation in the location of the peak between the A and the Q cases.

4 Discussion

4.1 Channel steepness index and Erosion Rates

Our numerical experiments show that in lithologically homogeneous landscapes it is possible to distinguish between drainage area and discharge-driven landscapes from topographic metrics alone. If the imposed incision law is discharge-driven, but channel steepness is calculated assuming an area-driven incision driver (that is, χ is calculated only taking A into account), the distortions to the channel steepness index can be as high as 34% within our simulations, with varying patterns depending on the lithology and the type of rainfall. Homogeneous lithology leads to k_{sn} distortion that increases monotonically with increasing rainfall ranges (Figure 4A, C, D), whereas heterogeneous lithologies totally overprint rainfall-related signals (see Figure 6A, B, C). Adding heterogeneous lithologies in the model simulations also induces a systematic increase in the disorder metric. This makes it harder to identify a pattern whereby a worker can clearly extract

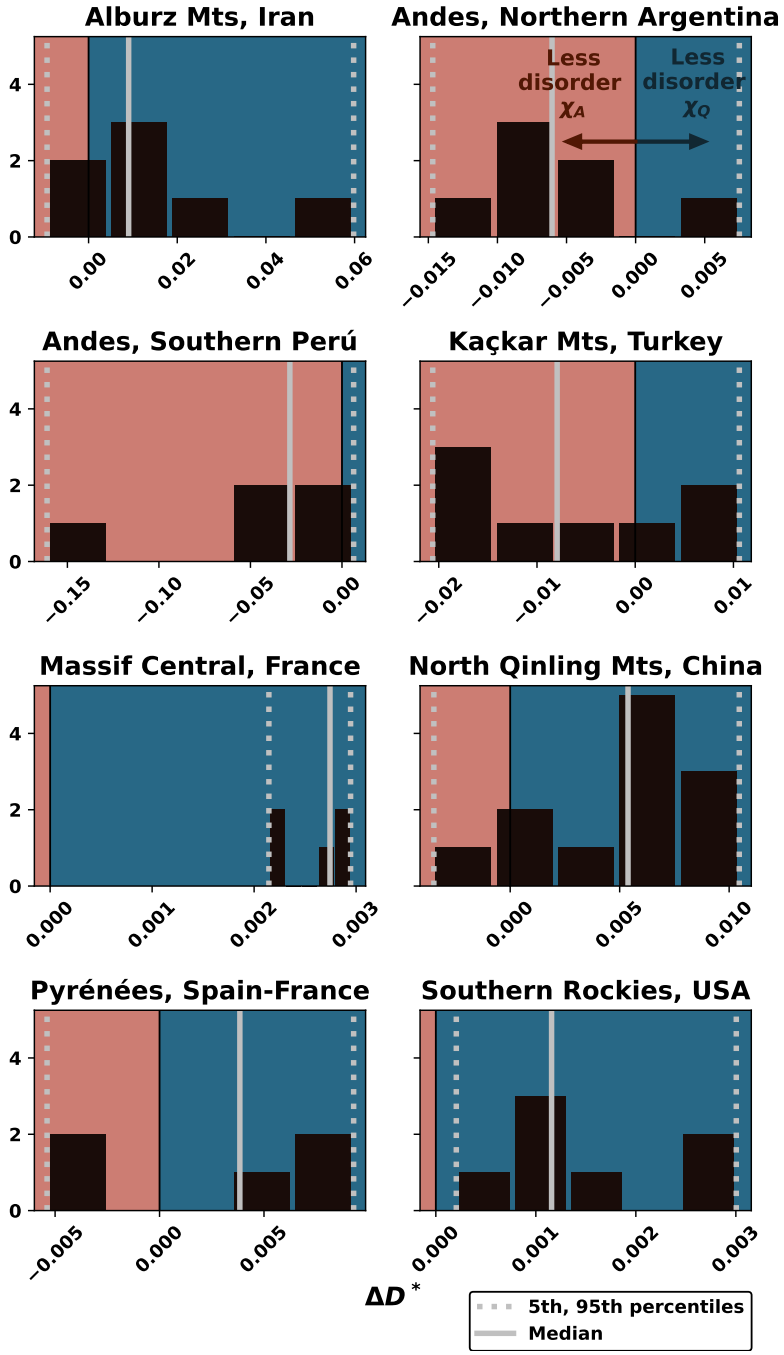

Figure 7. Comparison of the median values for ΔD^* for each of the mountain ranges. Results that lie above the y=0 line correspond to cases driven by rainfall. Points that lie below the y=0 line are cases where other forcings aside from rainfall(such as tectonics or lithology) are dominating over the rainfall signal. Some cases show a slight preference towards χ_A (Perú, Argentina, Turkey) whereas the rest prefer χ_Q. However, the confidence interval for this is lower than 95%, meaning that the results are largely basin dependent. Topographic analysis is not sufficient to draw conclusions about the incision mechanisms and further field observations of erosion rates would be needed.

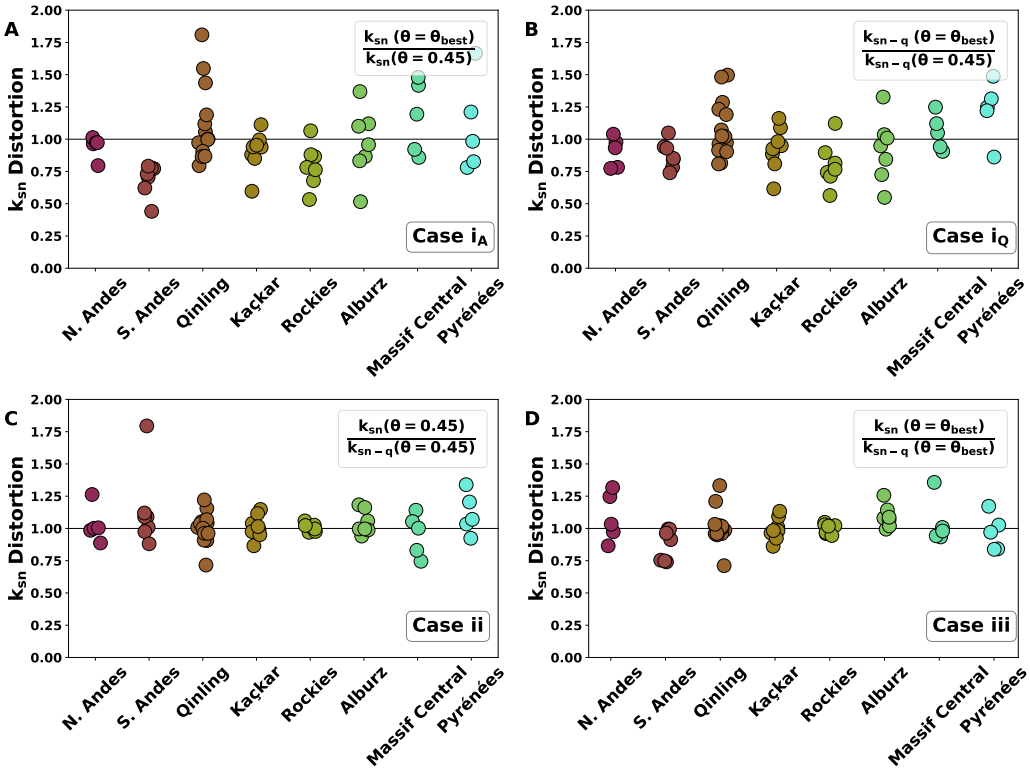

Figure 8. Distortion in k_{sn} for a range of natural landscapes. A distortion of 1 (solid black line) keeps the value of k_{sn} unchanged. The distortion scenarios are a representation of how one might introduce bias in k_{sn} under an unknown incision scenario, as is the case in many sites. Keeping θ=0.45 under different incision scenarios can lead to distortions of up to 79% (C). We show as well the distortion introduced by choosing θ=0.45 instead of θ_{best}, reaching 81% under A-driven incision (A) and 50% under Q-driven incision (B). (D) depicts the distortion introduced by optimizing θ under both incision regimes, with values of up to 36%.

the range of rainfall across the mountain range. For instance, in the striped lithology case (Figure S2, SI) all basins are affected by both the two erodibilities and the rainfall ranges, but at different parts of the catchment, because some tributaries will only have one rock type.

Distortions in channel steepness index are not solely caused by external forcings, such as rainfall or erodibility. In simulations depicted in Figure 4 we have imposed a discharge-driven incision rule, with a θ of 0.45. The largest distortions result from comparing the imposed incision law with the correct θ against the incorrect incision law with an optimized θ (Figure 4D). However, in a real landscape we will not know the "true" erosion law or the "true" value of θ, and we find that the distortions associated with changing the θ value between 0.45 (used in many studies) and an optimized θ is similar to the distortions introduced by not accounting for rainfall (Figure 4A and C).

A change in distortion is a reflection of differences between tributaries and trunk behavior as a result of spatial changes in rainfall. For instance, tributaries represent a larger percentage of the channels in smaller basins, meaning that their signal becomes amplified in those cases (Leonard et al., 2023). We then expect different parts of the catchment and channels of different sizes to react differently to spatially heterogenous rain-

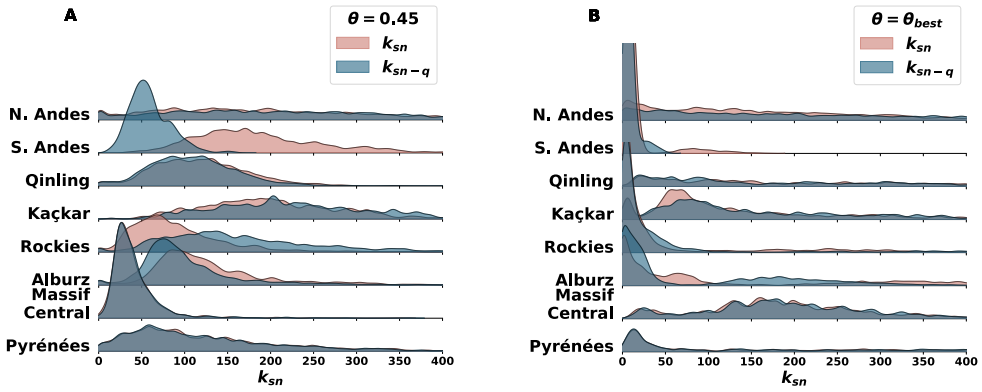

Figure 9. Distribution of k_{sn} and k_{sn-q} values for all the basins across each mountain range. Assuming θ=0.45, we see large difference in k_{sn} values and distribution shape for the Southern Andes and the Rockies, other areas, such as the Massif Central or the Pyrénées do not experience significant changes. Under θ_{best} (B), the distribution largely changes from (A), shifting towards smaller channel steepness index. Mountain ranges like the Rockies now show a closer agreement between the k_{sn} and the k_{sn-q} distributions.

fall and lithology. According to the modeling work by Han et al. (2015), smaller channels are more affected by rainfall, with large variability in k_{sn} reflecting the precipitation gradient. Recent work by Leonard et al. (2023) proposes that smaller catchments are more prone to biases because their contribution to the overall basin metrics is larger. In line with this, we have set bounds for basin drainage area size and minimum tributary size. This will lead to more consistent k_{sn} values and avoid incorporating tributaries dominated by hillslope diffusivity processes. Our modeling results suggest that in Q-driven basins, given that the concavity index is optimized, the distortion will be minimal when using k_{sn-q}. This is agrees with the study by Leonard et al. (2023), where in areas of the Andean Cordillera with strong rainfall gradients k_{sn-q} and $\theta_{ref} = 0.50$ yield a minimal distortion.

Natural topography, however, shows more complexity than our sandbox models, which leads to difficulties in identifying the different incision scenarios. We choose a small number of basins across a multitude of different areas (as opposed to (Leonard et al., 2023), where the study is along a single geographical region) to identify topographic metrics than can differentiate between incision scenarios. This offers the worker an estimate of how much of a distortion they would introduce given the incorrect incision rule or concavity index. Leonard et al. (2023) also show that in the Andes, the differences between the trunk and tributaries are starker when using the incorrect incision mechanism than when comparing k_{sn} under different -incorrect- concavity index scenarios.

Determining the incision rule that is more consistent with observed topography will help in interpreting topography in areas with large changes in rainfall across the study area. The distortion that we have found in our study can then be translated into uncertainties in erosion rates. (Adams et al., 2020) found that the erosion rates from Be-10

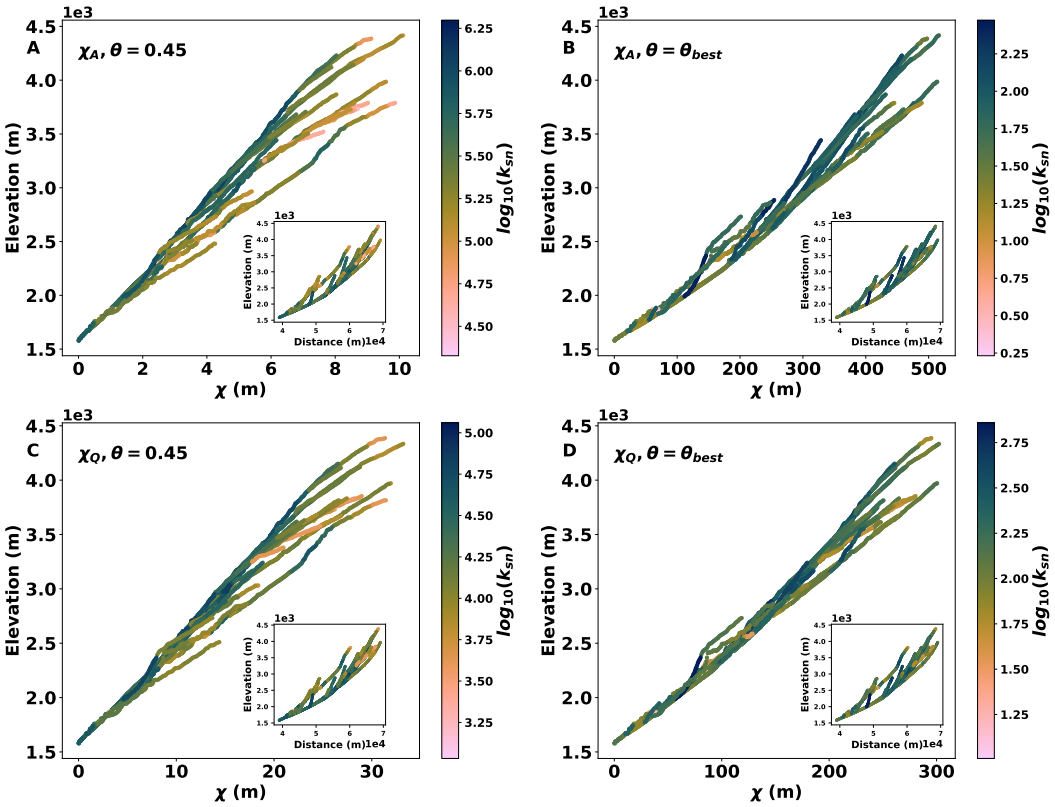

Figure 10. χ profiles for a basin in the Argentinian Andes, under different incision and concavity index scenarios. The disorder decreases when we optimize the concavity index (θ_{best}) ((B) and (D)). The channel steepness index is higher when θ=0.45 ((A) and (C)). Compared to the effects that changes in concavity index have in the profiles, the choice of incision rule introduce secondary differences in the channels.

in the Himalayas and Bhutan are better constrained when using k_{sn-q} instead of k_{sn} (which (Leonard et al., 2023) corroborates), otherwise causing them to be artificially high. We find that changes in the concavity index can lead to changes in channel steepness index which are often larger than those caused by spatially varying rainfall, suggesting a potential cumulative effect of the different biases.

However, these changes in θ values are linked not only to different rainfall (Harries et al., 2021; Zaprowski et al., 2005) and lithological regimes (Duvall et al., 2004). The nature of the river bed (Howard & Kerby, 1983; Tucker & Whipple, 2002), the sediment availability (Wickert & Schildgen, 2019), and the tectonic setting (Kirby & Whipple, 2001) can also affect the value of θ in different reaches of the rivers in a way that would become hard to disentangle from spatial changes in rainfall. Han et al. (2015) explores changes that spatially varied rainfall can have on the concavity index through modeling experiments. In natural landscapes, changes around their chosen value of 0.5 vary comparatively less due to rain gradients than changes caused by factors such as the type of channel bed (Whipple & Tucker, 2002), sediment amounts (Gasparini et al., 2007) or uplift rate changes (Kirby & Whipple, 2001).

The distribution of k_{sn} and k_{sn-q} values for natural landscapes shows the variability in behavior between mountain ranges (Figure 9). For $\theta = \theta_{best}$, the variability between k_{sn} and k_{sn-q} is smaller than for $\theta = 0.45$. This means that as long as the con-

cavity index has been constrained, the channel steepness index variations between A and Q-scenarios will be smaller than if $\theta = 0.45$ was chosen. We note that the mountain ranges where the distributions diverge for A and Q cases often correspond to the ones where the disorder is high, demonstrating once more that using unconstrained values of *theta* to extract geomorphometrics can amplify process-linked biases. For instance Argentina shows consistently distortion between 25-75% in Figure 8, seeing some of the largest variability in channel steepness index for some of the basins. Plotting the χ-elevation plots for one of the basins with the strongest distortion Figure 10, we can see that the disorder of the tributaries with respect to the main stem is decreased the most when using χ_Q and $\theta = \theta_{best}$. Most of the changes in channel steepness index due to concavity index optimization affect the upstream tributaries, we see as well how the profiles collapse more as a result of choosing θ_{best} than by including or removing rainfall in the calculations.

4.2 Rainfall and climate

In this work, we have chosen to simplify the rainfall patterns in manner mirroring (Leonard & Whipple, 2021) by approximating the orographic behavior using a linear increase of rainfall with distance along the mountain range, emulating the effect that orographic rainfall has on real landscapes. The rainfall asymmetry generates a displacement of the divide towards the drier side of the mountain, where the erosion is smaller. We observe different levels of channel steepness index distortion for the wet and the dry side of the simulated mountain ranges, and making it possible to identify the type of rainfall gradient (top-heavy or bottom-heavy - following the nomenclature in (Leonard & Whipple, 2021)- from the value of the distortion ratio. This difference between the wet and the dry side of natural landscapes has been studied in depth in natural settings such as Hawai'i (Ferrier et al., 2013), albeit in tectonically complex regions outside our scope.

In the modeling framework, we have assumed that the rainfall pattern remains constant throughout time, but this is not necessarily the case in natural landscapes. Even small climate changes can lead to changes in the rainfall pattern and discharge amounts at different parts of the catchment, altering the local erosion rates and displacing the landscape from an equilibrium state (Leonard & Whipple, 2021). The regions of study lie within the mid-latitudes, where the climate has remained largely unchanged (Roe et al., 2002). Changes in atmospheric circulation patterns or temperature changes (Herman et al., 2013; Bradley, 2015; Ward & Galewsky, 2014) are some examples of cases when other climate variable can affect erosion rates. Glaciations are also important when considering a large portion of the Earth's landscapes, and they also show a relation with the erosion rates and the relief of the landscape. From our simulations, we have seen how the relief decreases as precipitation rates increase, as expected. In natural landscapes, the relationship between relief and rainfall is complex and influenced by local processes beyond the scope of this project (Montgomery et al., 2001; Champagnac et al., 2012).

4.3 Disorder to indicate incision rate

Our hypothesis states that basins undergoing a strong rainfall gradient are distinguishable based on their disorder values. This is true under homogeneous lithologies and in cases where the erodibility differences happen smoothly over the scale of multiple basins. In this case, it is possible to distinguish with 95% confidence between A-driven incision and Q-driven incision, regardless of the rainfall gradient. Adding sudden changes in lithology within basins and natural topographies makes identifying the correct incision rule challenging. The shape of the basins can have an effect on the disorder values. (Han et al., 2015) highlight how longer and narrower catchments experience a similar rainfall gradient between the tributaries and the trunk channel, whereas wider basins where the tributaries are more misaligned experience a higher disorder. In our experiments, we are looking at the overall behavior of the landscape, thus mixing basin shapes which would in-

trinsically have different disorders based on their shape, regardless of the forcing. Since in the disorder calculations we only compare each basin with itself under different incision scenarios, the intrinsic disorder differences between basins should not pose a bias.

4.4 Limitations

One of the limitations of our study lies in the precipitation treatment, both in the modeling study and in the natural landscapes. While it is possible to reproduce a realistic rainfall pattern using the Fastscape module adapted from (Smith & Barstad, 2004), it is computationally expensive and requires knowledge of the wind patterns of the region of interest, which change at different atmospheric layers. We assume that the orographic rainfall can be approximated in the modeling framework by a linear rainfall trend that does not change through the simulation, regardless of the relief (Roe et al., 2003). In real orographic rainfall scenarios, there would be a positive feedback between the rainfall and the topography, which our model does not capture.

In our natural sites, we also assume that the rainfall pattern, derived from the average rainfall from 20 years (2000-2020), is representative of the precipitation at that site throughout its history, in geologic timescales. Climate patterns have changed throughout the centuries driven by changes in atmospheric condition, solar irradiance, and biosphere and ocean changes (Bradley, 2015). The regions of study lie within the mid-latitudes, where the climate has remained largely unchanged (Roe et al., 2002). However, due to having taken into account data from the 21st century, recent changes in rainfall pattern due to human made climate change cannot be ruled out to have intervened in the data from the past years compared to data prior to industrial revolution.

The question of whether mean annual precipitation should be used to describe the climate of a region is also a highly debated topic, with studies suggesting that it is the storms and extreme events which contribute the most to mean annual precipitation and do the most erosive work (Sorensen & Yanites, 2019; DiBiase & Whipple, 2011; Deal et al., 2017, 2018; Rasmussen et al., 2016). Other studies prefer the use of mean annual precipitation (Leonard & Whipple, 2021; Adams et al., 2020; Rossi et al., 2016; Anders et al., 2006; D'Arcy & Whittaker, 2014; Gasparini & Whipple, 2014; Armitage et al., 2011), especially when capturing the erosion work longer climatic trend or incorporating it in long-term landscape evolution models.

In the modeling framework, many processes have been simplified. We have already mentioned the rainfall patterns, which is the main focus of this study. The representation of lithological units, the exclusion of sediment supply and the homogeneous uplift, have all been choices made to isolate the climatic signal as much as possible. We are also assuming that the detachment limited SPM forms a good basis for how rainfall interacts with uplift and erosion, which many studies support (e.g., Leonard et al., 2023; Leonard & Whipple, 2021; Adams et al., 2020; Gasparini & Whipple, 2014; Harries et al., 2021), while acknowledging it still does not fully explain all geomorphic processes at the landscape scale.

5 Conclusions

In this study, we explore whether it is possible to determine whether channel incision is most closely related to drainage area or discharge (or some proxy thereof) from topographic metrics alone. Many past papers quantify channel steepness calculated based on drainage area as an indicator of river incision rates (e.g., Kirby & Whipple, 2012; Harel et al., 2016), but now that precipitation records are more readily available (Skofronick-Jackson et al., 2017), we must question whether adding rainfall gradients to the equation will yield different topographic outcomes in river channels.

In a simple numerical model with homogeneous lithology, disorder metrics (Mudd et al., 2018; Gailleton et al., 2021; Goren et al., 2014) yield a clear distinction between A and Q-driven incision basins with a monotonic dependence on rainfall gradients. When the system is perturbed by adding areas with different erodibilities, the incision signal is obscured. However, including rainfall gradients is not the only way to distort a signal. We have quantified the effects that optimizing the concavity index θ can have in the channels, concluding that using the standard value of $\theta = 0.45$ amplifies the distortion caused by rainfall effects.

In natural landscapes, we cannot establish a general topographic rule to distinguish between A and Q-shaped basins. We find catchments that are better described by discharge and others by drainage area, in some cases with quite a stark contrast. Given that we are not able to separate those cases topographically, we quantify how much distortion we would introduce in channel steepness index if we failed to identify the incision mechanism. Our results suggest that in most basins we would see maximum changes in channel steepness index of up to 25%, which does not constitute enough to drastically change the interpretation of erosion rates across the landscape. We compare this to distortions in k_{sn} of 50% obtained from using $\theta = 0.45$ instead of optimizing the concavity index. We suggest readers to use θ_{best} as an efficient method to reduce distortions already introduced by an unknown incision mechanism.

6 Open Research

Analyses have been run using open source software (lsdtopotools v0.9, lsdtopytools). Precipitation data was retrieved using the package gpm_precipitation_tools. Visualization scripts and model workflows are available in the Github repository `https://github.com/MarinaRuizSO/JGR_paper`, which will be archived and assigned a doi if the manuscript is accepted for publication.

Acknowledgments

Funding for MRSO was provided by the Natural Environment Research Council (NERC NE/S007407/1). This research has been supported by the H2020 European Research Council (grant no. 803721). Perceptually uniform scientific color maps (Crameri, 2023) are used in this study to prevent visual distortion of the data and exclusion of readers with color-vision deficiencies (Crameri et al., 2020).

References

Adams, B. A., Whipple, K. X., Forte, A. M., Heimsath, A. M., & Hodges, K. V. (2020). Climate controls on erosion in tectonically active landscapes. *Science Advances*, *6*, 3166–3182. doi: 10.1126/sciadv.aaz3166

Anders, A. M., Roe, G. H., Hallet, B., Montgomery, D. R., Finnegan, N. J., & Putkonen, J. (2006). Spatial patterns of precipitation and topography in the Himalaya. *Special Paper of the Geological Society of America*, *398*, 39–53. doi: 10.1130/2006.2398(03)

Armitage, J. J., Duller, R. A., Whittaker, A. C., & Allen, P. A. (2011). Transformation of tectonic and climatic signals from source to sedimentary archive. *Nature Geoscience*, *4*(4), 231–235. doi: 10.1038/ngeo1087

Babault, J., Viaplana-Muzas, M., Legrand, X., Van Den Driessche, J., González-Quijano, M., & Mudd, S. M. (2018). Source-to-sink constraints on tectonic and sedimentary evolution of the western Central Range and Cenderawasih Bay (Indonesia). *Journal of Asian Earth Sciences*, *156*, 265–287. doi: 10.1016/j.jseaes.2018.02.004

Baynes, E. R., Lague, D., Steer, P., Bonnet, S., & Illien, L. (2020). Sediment flux-

driven channel geometry adjustment of bedrock and mixed gravel–bedrock rivers. *Earth Surface Processes and Landforms*, *45*(14), 3714-3731. doi: 10.1002/esp.4996

Bernard, T., Sinclair, H. D., Gailleton, B., & Fox, M. (2021). Formation of Longitudinal River Valleys and the Fixing of Drainage Divides in Response to Exhumation of Crystalline Basement. *Geophysical Research Letters*, *48*(8), e2020GL092210. doi: 10.1029/2020GL092210

Bookhagen, B., & Burbank, D. W. (2006). Topography, relief, and TRMM-derived rainfall variations along the Himalaya. *Geophysical Research Letters*, *33*(8), L08405. doi: 10.1029/2006GL026037

Bookhagen, B., & Strecker, M. R. (2008). Orographic barriers, high-resolution TRMM rainfall, and relief variations along the eastern Andes. *Geophysical Research Letters*, *35*(6), L06403. doi: 10.1029/2007GL032011

Bovy, B., & Lange, R. (2023). *fastscape-lem/fastscape: Release v0.1.0.* Zenodo. doi: 10.5281/ZENODO.8375653

Bradley, R. S. (2015). Climate and Climatic Variation. *Paleoclimatology*, 13–54. doi: 10.1016/B978-0-12-386913-5.00002-8

Braun, J., & Willett, S. D. (2013). A very efficient O(n), implicit and parallel method to solve the stream power equation governing fluvial incision and landscape evolution. *Geomorphology*, *180-181*, 170–179. doi: 10.1016/j.geomorph.2012.10.008

Champagnac, J.-D., Molnar, P., Sue, C., & Herman, F. (2012). Tectonics, climate, and mountain topography. *Journal of Geophysical Research: Solid Earth*, *117*(B2). doi: 10.1029/2011JB008348

Cox, N. J. (2007). Kernel estimation as a basic tool for geomorphological data analysis. *Earth Surface Processes and Landforms*, *32*(12), 1902-1912. doi: 10.1002/esp.1518

Craddock, W. H., Burbank, D. W., Bookhagen, B., & Gabet, E. J. (2007). Bedrock channel geometry along an orographic rainfall gradient in the upper Marsyandi River valley in central Nepal. *Journal of Geophysical Research: Earth Surface*, *112*(3). doi: 10.1029/2006JF000589

Crameri, F. (2023). *Scientific colour maps.* Zenodo. doi: 10.5281/zenodo.8409685

Crameri, F., Shephard, G. E., & Heron, P. J. (2020). The misuse of colour in science communication. *Nature Communications*, *11*. doi: 10.1038/s41467-020-19160-7

D'Arcy, M., & Whittaker, A. C. (2014). Geomorphic constraints on landscape sensitivity to climate in tectonically active areas. *Geomorphology*, *204*, 366–381. doi: 10.1016/j.geomorph.2013.08.019

Deal, E., Braun, J., & Botter, G. (2018). Understanding the Role of Rainfall and Hydrology in Determining Fluvial Erosion Efficiency. *Journal of Geophysical Research: Earth Surface*, *123*(4), 744–778. doi: 10.1002/2017JF004393

Deal, E., Favre, A.-C., & Braun, J. (2017). Rainfall variability in the Himalayan orogen and its relevance to erosion processes. *Water Resources Research*, *53*(5), 4004–4021. doi: 10.1002/2016WR020030

DiBiase, R. A., & Whipple, K. X. (2011). The influence of erosion thresholds and runoff variability on the relationships among topography, climate, and erosion rate. *Journal of Geophysical Research: Earth Surface*, *116*(F4), 4036. doi: 10.1029/2011JF002095

DiBiase, R. A., Whipple, K. X., Heimsath, A. M., & Ouimet, W. B. (2010). Landscape form and millennial erosion rates in the San Gabriel Mountains, CA. *Earth and Planetary Science Letters*, *289*(1-2), 134–144. doi: 10.1016/J.EPSL.2009.10.036

Dunne, K. B. J., & Jerolmack, D. J. (2020). What sets river width? *Science Advances*, *6*(41), eabc1505. doi: 10.1126/sciadv.abc1505

Duvall, A., Kirby, E., Burbank, D., Duvall, C. ., Kirby, E., & Burbank, D. (2004).

Tectonic and lithologic controls on bedrock channel profiles and processes in coastal California. *Journal of Geophysical Research: Earth Surface*, *109*(F3), 3002. doi: 10.1029/2003JF000086

Ferrier, K. L., Huppert, K. L., & Perron, J. T. (2013). Climatic control of bedrock river incision. *Nature*, *496*(7444), 206–209. doi: 10.1038/nature11982

Finnegan, N. J., Sklar, L. S., & Fuller, T. K. (2007). Interplay of sediment supply, river incision, and channel morphology revealed by the transient evolution of an experimental bedrock channel. *Journal of Geophysical Research: Earth Surface*, *112*(F3). doi: 10.1029/2006JF000569

Flint, J. J. (1974). Stream gradient as a function of order, magnitude, and discharge. *Water Resources Research*, *10*(5), 969–973. doi: 10.1029/WR010i005p00969

Forte, A. M., Yanites, B. J., & Whipple, K. X. (2016). Complexities of landscape evolution during incision through layered stratigraphy with contrasts in rock strength. *Earth Surface Processes and Landforms*, *41*(12), 1736–1757. doi: 10.1002/esp.3947

Fournier, A., Fussell, D., & Carpenter, L. (1982). Computer Rendering of Stochastic Models. *Commun. ACM*, *25*(6), 371–384. doi: 10.1145/358523.358553

Gailleton, B., Mudd, S. M., Clubb, F. J., Grieve, S. W., & Hurst, M. D. (2021). Impact of Changing Concavity Indices on Channel Steepness and Divide Migration Metrics. *Journal of Geophysical Research: Earth Surface*, *126*(10). doi: 10.1029/2020JF006060

Gasparini, N. M., & Brandon, M. T. (2011). A generalized power law approximation for fluvial incision of bedrock channels. *Journal of Geophysical Research: Earth Surface*, *116*(2), 1–16. doi: 10.1029/2009JF001655

Gasparini, N. M., & Whipple, K. X. (2014). Diagnosing climatic and tectonic controls on topography: Eastern flank of the northern Bolivian Andes. *Lithosphere*, *6*(4). doi: 10.1130/L322.1

Gasparini, N. M., Whipple, K. X., & Bras, R. L. (2007). Predictions of steady state and transient landscape morphology using sediment-flux-dependent river incision models. *Journal of Geophysical Research*, *112*(F3), F03S09. doi: 10.1029/2006JF000567

Gilbert, G. (1877). *Geology of the Henry Mountains* (Tech. Rep.). Washington, D.C.: Government Printing Office.

Goren, L., Fox, M., & Willett, S. D. (2014). Tectonics from fluvial topography using formal linear inversion: Theory and applications to the Inyo Mountains, California. *Journal of Geophysical Research: Earth Surface*, *119*(8), 1651–1681. doi: 10.1002/2014JF003079

Grujic, D., Govin, G., Barrier, L., Bookhagen, B., Coutand, I., Cowan, B., ... Najman, Y. (2018). Formation of a Rain Shadow: O and H Stable Isotope Records in Authigenic Clays From the Siwalik Group in Eastern Bhutan. *Geochemistry, Geophysics, Geosystems*, *19*(9), 3430–3447. doi: 10.1029/2017GC007254

Hack, J. T. (1960). Interpretation of erosional topography in humid temperate regions. *American Journal of Science*, *258*(A), 80–97.

Han, J., Gasparini, N. M., & Johnson, J. P. (2015). Measuring the imprint of orographic rainfall gradients on the morphology of steady-state numerical fluvial landscapes. *Earth Surface Processes and Landforms*, *40*(10), 1334–1350. doi: 10.1002/esp.3723

Harel, M. A., Mudd, S. M., & Attal, M. (2016). Global analysis of the stream power law parameters based on worldwide 10Be denudation rates. *Geomorphology*, *268*, 184–196. doi: 10.1016/j.geomorph.2016.05.035

Harries, R. M., Gailleton, B., Kirstein, L. A., Attal, M., Whittaker, A. C., & Mudd, S. M. (2021). Impact of climate on landscape form, sediment transfer and the sedimentary record. *Earth Surface Processes and Landforms*, *46*(5), 990–1006. doi: 10.1002/esp.5075

Hergarten, S., & Robl, J. (2022). The linear feedback precipitation model (LFPM

1.0) – a simple and efficient model for orographic precipitation in the context of landform evolution modeling. *Geoscientific Model Development*, *15*(5), 2063–2084. doi: 10.5194/gmd-15-2063-2022

Hergarten, S., Robl, J., & Stüwe, K. (2016). Tectonic geomorphology at small catchment sizes-extensions of the stream-power approach and the χ method. *Earth Surface Dynamics*, *4*, 1–9. doi: 10.5194/esurf-4-1-2016

Herman, F., Seward, D., Valla, P. G., Carter, A., Kohn, B., Willett, S. D., & Ehlers, T. A. (2013). Worldwide acceleration of mountain erosion under a cooling climate. *Nature*, *504*(7480), 423–426. doi: 10.1038/nature12877

Howard, A. D. (1987). Modelling fluvial systems: rock-, gravel- and sand-bed channels. In K. Richards (Ed.), *River channels* (p. 69-94). Oxford: Basil Blackwell.

Howard, A. D., & Kerby, G. (1983). Channel changes in badlands. *GSA Bulletin*, *94*(6), 739–752. doi: 10.1130/0016-7606(1983)94⟨739:CCIB⟩2.0.CO;2

Johnson, J. P. L., & Whipple, K. X. (2010). Evaluating the controls of shear stress, sediment supply, alluvial cover, and channel morphology on experimental bedrock incision rate. *Journal of Geophysical Research: Earth Surface*, *115*(F2). doi: 10.1029/2009JF001335

Kirby, E., & Whipple, K. (2001). Quantifying differential rock-uplift rates via stream profile analysis. *Geology*, *29*(5), 415–418. doi: 10.1130/0091-7613(2001)029⟨0415:QDRURV⟩2.0.CO;2

Kirby, E., & Whipple, K. X. (2012). Expression of active tectonics in erosional landscapes. *Journal of Structural Geology*, *44*, 54–75. doi: 10.1016/J.JSG.2012.07.009

Kummerow, C., Simpson, J., Thiele, O., Barnes, W., Chang, A. T., Stocker, E., ... Nakamura, K. (2000). The status of the tropical rainfall measuring mission (TRMM) after two years in orbit. *Journal of Applied Meteorology*, *39*(12 PART 1), 1965–1982. doi: 10.1175/1520-0450(2001)040⟨1965:tsottr⟩2.0.co;2

Lague, D. (2014). The stream power river incision model: Evidence, theory and beyond. *Earth Surface Processes and Landforms*, *39*(1), 38–61. doi: 10.1002/esp.3462

Leonard, J. S., & Whipple, K. X. (2021). Influence of spatial rainfall gradients on river longitudinal profiles and the topographic expression of spatially and temporally variable climates in mountain landscapes. *Journal of Geophysical Research: Earth Surface*, *126*(12), e2021JF006183. doi: 10.1029/2021JF006183

Leonard, J. S., Whipple, K. X., & Heimsath, A. M. (2023). Isolating climatic, tectonic, and lithologic controls on mountain landscape evolution. *Science advances*, *9*(3), eadd8915. doi: 10.1126/sciadv.add8915

Montgomery, D. R., Balco, G., & Willett, S. D. (2001). Climate, tectonics, and the morphology of the Andes. *Geology*, *29*(7), 579–582. doi: 10.1130/0091-7613(2001)029⟨0579:CTATMO⟩2.0.CO;2

Morisawa, M. E. (1962). Quantitative Geomorphology of Some Watersheds in the Appalachian Plateau. *Geological Society of America Bulletin*, *73*(9), 1025–1046. doi: 10.1130/0016-7606(1962)73[1025:QGOSWI]2.0.CO;2

Mudd, S. M., Attal, M., Milodowski, D. T., Grieve, S. W., & Valters, D. A. (2014). A statistical framework to quantify spatial variation in channel gradients using the integral method of channel profile analysis. *Journal of Geophysical Research: Earth Surface*, *119*(2), 138–152. doi: 10.1002/2013JF002981

Mudd, S. M., Clubb, F. J., Gailleton, B., & Hurst, M. D. (2018). How concave are river channels? *Earth Surface Dynamics*, *6*(2), 505–523. doi: 10.5194/ESURF-6-505-2018

Peifer, D., Persano, C., Hurst, M. D., Bishop, P., & Fabel, D. (2021). Growing topography due to contrasting rock types in a tectonically dead landscape. *Earth Surface Dynamics*, *9*(2), 167–181. doi: 10.5194/ESURF-9-167-2021

Perlin, K. (1985). Image synthesizer. *Computer Graphics (ACM)*, *19*, 287-296. doi: 10.1145/325165.325247

Perron, J. T., & Royden, L. (2013). An integral approach to bedrock river profile analysis. *Earth Surface Processes and Landforms*, *38*(6), 570–576. doi: 10.1002/esp.3302

Pfeiffer, A. M., Finnegan, N. J., & Willenbring, J. K. (2017). Sediment supply controls equilibrium channel geometry in gravel rivers. *Proceedings of the National Academy of Sciences*, *114*(13), 3346-3351. doi: 10.1073/pnas.1612907114

Phillips, C. B., & Jerolmack, D. J. (2016). Self-organization of river channels as a critical filter on climate signals. *Science*, *352*(6286), 694-697. doi: 10.1126/science.aad3348

Rasmussen, K. L., Chaplin, M. M., Zuluaga, M. D., & Houze, R. A. (2016). Contribution of Extreme Convective Storms to Rainfall in South America. *Journal of Hydrometeorology*, *17*(1), 353–367. doi: 10.1175/JHM-D-15-0067.1

Roe, G. H., Montgomery, D. R., & Hallet, B. (2002). Effects of orographic precipitation variations on the concavity of steady-state river profiles. *Geology*, *30*(2), 143–146. doi: 10.1130/0091-7613(2002)030⟨0143:EOOPVO⟩2.0.CO;2

Roe, G. H., Montgomery, D. R., & Hallet, B. (2003). Orographic precipitation and the relief of mountain ranges. *Journal of Geophysical Research: Solid Earth*, *108*(B6), 2315. doi: 10.1029/2001JB001521

Rossi, M. W., Whipple, K. X., & Vivoni, E. R. (2016). Precipitation and evapotranspiration controls on daily runoff variability in the contiguous United States and Puerto Rico. *Journal of Geophysical Research: Earth Surface*, *121*(1). doi: 10.1002/2015JF003446

Royden, L., & Perron, J. T. (2013). Solutions of the stream power equation and application to the evolution of river longitudinal profiles. *Journal of Geophysical Research: Earth Surface*, *118*(2), 497-518. doi: 10.1002/jgrf.20031

Royden, L. H., Clark, M. K., & Whipple, K. X. (2000). Evolution of river elevation profiles by bedrock incision: Analytical solutions for transient river profiles related to changing uplift and precipitation rates. *Eos Trans. AGU, 81(48), Fall Meet. Suppl., Abstract T62F-09*. doi: 10.1002/eost.v81.16

Silverman, B. W. (1998). *Density estimation for statistics and data analysis*. Routledge. doi: 10.1201/9781315140919

Skofronick-Jackson, G., Petersen, W. A., Berg, W., Kidd, C., Stocker, E. F., Kirschbaum, D. B., ... Wilheit, T. (2017). The global precipitation measurement (GPM) mission for science and Society. *Bulletin of the American Meteorological Society*, *98*(8), 1679–1695. doi: 10.1175/BAMS-D-15-00306.1

Smith, R. B., & Barstad, I. (2004). A linear theory of orographic precipitation. *Journal of the Atmospheric Sciences*, *61*(12), 1377–1391. doi: 10.1175/1520-0469(2004)061⟨1377:ALTOOP⟩2.0.CO;2

Sorensen, C. S., & Yanites, B. J. (2019). Latitudinal trends in modern fluvial erosional efficiency along the Andes. *Geomorphology*, *329*, 170–183. doi: 10.1016/j.geomorph.2018.12.030

Tucker, G. E., & Whipple, K. X. (2002). Topographic outcomes predicted by stream erosion models: Sensitivity analysis and intermodel comparison. *Journal of Geophysical Research: Solid Earth*, *107*(B9), 1–1. doi: 10.1029/2001JB000162

Ward, D. J., & Galewsky, J. (2014). Exploring landscape sensitivity to the Pacific Trade Wind Inversion on the subsiding island of Hawaii. *Journal of Geophysical Research: Earth Surface*, *119*(9), 2048–2069. doi: 10.1002/2014JF003155

Whipple, K. X., & Tucker, G. E. (1999). Dynamics of the stream-power river incision model: Implications for height limits of mountain ranges, landscape response timescales, and research needs. *Journal of Geophysical Research: Solid Earth*, *104*(B8), 17661–17674. doi: 10.1029/1999JB900120

Whipple, K. X., & Tucker, G. E. (2002). Implications of sediment-flux-dependent river incision models for landscape evolution. *Journal of Geophysical Research: Solid Earth*, *107*(B2), 3–1. doi: 10.1029/2000JB000044

Wickert, A. D., & Schildgen, T. F. (2019). Long-profile evolution of transport-

limited gravel-bed rivers. *Earth Surface Dynamics*, *7*(1), 17–43. doi: 10.5194/ESURF-7-17-2019

Wobus, C. W., Tucker, G. E., & Anderson, R. S. (2006). Self-formed bedrock channels. *Geophysical Research Letters*, *33*(18), 18408. doi: 10.1029/2006GL027182

Wobus, C. W., Tucker, G. E., & Anderson, R. S. (2010). Does climate change create distinctive patterns of landscape incision? *Journal of Geophysical Research: Earth Surface*, *115*(4). doi: 10.1029/2009JF001562

Zaprowski, B. J., Pazzaglia, F. J., & Evenson, E. B. (2005). Climatic influences on profile concavity and river incision. *Journal of Geophysical Research: Earth Surface*, *110*(F3), 3004. doi: 10.1029/2004JF000138